















# Developing Atom Probe Tomography of Phyllosilicates in Preparation for Extra-Terrestrial Sample Return

Luke Daly (1, 2, 3, 4)\* , Martin R. Lee (1) , James R. Darling (5) , Ingrid McCarroll (2) , Limei Yang (2) , Julie Cairney (2, 6) , Lucy V. Forman (3, 7) , Phillip A. Bland (3) , Gretchen K. Benedix (3) , Denis Fougereuse (3, 8) , William D. A. Rickard (8) , David W. Saxey (8) , Steven M. Reddy (3, 8) , William Smith (9) and Paul A. J. Bagot (4) 

(1) School of Geographical and Earth Sciences, University of Glasgow, Glasgow G12 8QQ, UK

(2) Australian Centre for Microscopy and Microanalysis, University of Sydney, Sydney 2006, Australia

(3) Space Science and Technology Centre, School of Earth and Planetary Science, Curtin University, Bentley 6102, Australia

(4) Department of Materials, University of Oxford, Oxford OX1 3PH, UK

(5) School of the Environment, Geography and Geosciences, University of Portsmouth, Portsmouth PO1 3QL, UK

(6) School of Aerospace, Mechanical and Mechatronic Engineering, University of Sydney, Sydney 2006, Australia

(7) Department of Earth and Planetary Sciences, Western Australian Museum, Locked Bag 49, Welshpool 6986, Australia

(8) Geoscience Atom Probe Facility, John de Laeter Centre, Curtin University, GPO Box U1987, Perth 6845, Australia

(9) Materials and Condensed Matter Physics, School of Physics and Astronomy, University of Glasgow, Glasgow G12 8QQ, UK

\* Corresponding author. e-mail: luke.daly@glasgow.ac.uk

Hydrous phyllosilicate minerals, including the serpentine subgroup, are likely to be major constituents of material that will be brought back to Earth by missions to Mars and to primitive asteroids Ryugu and Bennu. Small quantities (< 60 g) of micrometre-sized, internally heterogeneous material will be available for study, requiring minimally destructive techniques. Many conventional methods are unsuitable for phyllosilicates as they are typically finely crystalline and electron beam-sensitive resulting in amorphisation and dehydration. New tools will be required for nanoscale characterisation of these precious extra-terrestrial samples. Here we test the effectiveness of atom probe tomography (APT) for this purpose. Using lizardite from the Ronda peridotite, Spain, as a terrestrial analogue, we outline an effective analytical protocol to extract nanoscale chemical and structural measurements of phyllosilicates. The potential of APT is demonstrated by the unexpected finding that the Ronda lizardite contains SiO-rich nanophases, consistent with opaline silica that formed as a by-product of the serpentinisation of olivine. Our new APT approach unlocks previously unobservable nanominerals and nanostructures within phyllosilicates owing to resolution limitations of more established imaging techniques. APT will provide unique insights into the processes and products of water/rock interaction on Earth, Mars and primitive asteroids.

Keywords: serpentinisation, atom probe tomography, asteroid sample return missions, nanomineralogy, fluid, rock interactions, Ryugu, transmission electron microscopy.

Received 15 Dec 20 – Accepted 15 Mar 21

Phyllosilicate minerals are characteristic products of the alteration of silicate rocks by aqueous solutions. These hydrous minerals form at the Earth's surface, for example during weathering and soil formation (e.g., Wilson 1999), and in the shallow crust under regimes including the diagenesis of sedimentary rocks (Wilson and Pittman 1977), and hydrothermal alteration of igneous rocks (e.g., Shau and Peacor 1992). In addition to demonstrating the presence of liquid water, the chemical and isotopic compositions of phyllosilicates can be used to constrain the physicochemical

conditions and provenance of the aqueous solutions (Hallis *et al.* 2012). These minerals also occur in extra-terrestrial contexts, where they are powerful indicators of water–rock interaction. Phyllosilicates have been identified by spectroscopic analysis of primitive asteroids (Rivkin *et al.* 2015) and by laboratory analysis of ordinary and carbonaceous chondrite meteorites (Barber 1981, Hutchison *et al.* 1987). Minerals including nontronite, montmorillonite and those of the serpentine subgroup have been shown to occur at the surface of Mars and in the planet's crust by using orbital

doi: 10.1111/ggr.12382

© 2021 The Authors. *Geostandards and Geoanalytical Research* published by John Wiley & Sons Ltd  
on behalf of the International Association of Geoanalysts

This is an open access article under the terms of the Creative Commons Attribution License,  
which permits use, distribution and reproduction in any medium, provided the original work is properly cited.

remote sensing (Poulet *et al.* 2005, Ehlmann *et al.* 2010), analysis by landers (e.g., Banin and Margulies 1983) and laboratory investigations of Martian meteorites (Bunch and Reid 1975, Lee *et al.* 2015a).

Here we focus on the fluid alteration product of olivine: serpentine, a suite of hydrated minerals spanning Fe- and Mg-rich varieties, which are a major constituent of Martian meteorite fluid alteration products (Bunch and Reid 1975, Lee *et al.* 2015a) and of the Mighei-like (CM) carbonaceous chondrite meteorites (Barber 1981, Dodd 1981, Hutchison 2006, Velbel *et al.* 2012). The CMs are the most abundant group of carbonaceous chondrites and are derived from one or more C-complex asteroids (Bunch and Chang 1980, Lee *et al.* 2019a). Because this phyllosilicate was formed by the action of water in asteroid interiors ~ 4563 million years ago (Fujiya *et al.* 2012), it is the oldest hydrous mineral available for study and gives unique insights into the solar system's earliest geological processes, including the origin of water and its delivery to Earth. The provenance and history of these serpentine-bearing meteorites will be much better constrained when samples are returned in the near future from two C-complex asteroids that have spectroscopic affinities to the CMs: the Cb-type asteroid (162173) Ryugu and the B-type asteroid (101955) Bennu (Hamilton *et al.* 2019, Kitazato *et al.* 2019).

As carbonaceous chondrite serpentine can reveal much about the nature of primordial water/rock interactions, it has been studied extensively using a variety of techniques. They include X-ray diffraction (Howard *et al.* 2015), electron and ion probe microanalysis (e.g., Velbel *et al.* 2012), transmission electron microscopy (TEM; e.g., Barber 1981) and low-voltage scanning TEM (Lee and Smith 2006). While these techniques provide a wealth of mineralogical and chemical data to characterise CM phyllosilicates, their applications are limited by the susceptibility of hydrous phases to electron beam damage (e.g., Barber 1981, Tomeoka and Buseck 1985, Lee and Lindgren 2016), which quickly results in amorphisation of the crystal structure, dehydration and devolatilisation of the mineral, and eventual destruction, allowing minimal time for analysis. In addition, these minerals are structurally weak and degrade rapidly. As such, analyses of this kind are very challenging. Only very small quantities (100 mg to 60 g) of material will be returned from Ryugu and Bennu (Tsuda *et al.* 2013, Lauretta *et al.* 2017, Sawada *et al.* 2017), consisting of micrometre-sized particles that are likely to be internally chemically, structurally and isotopically heterogeneous. Conventional techniques for bulk processing and analysis of phyllosilicates will have limited applicability for these samples because targeted sample preparation is needed. Thus, there is a

pressing need to develop new ways to maximise the information that can be obtained from the returned samples that destroys as little material as possible. Here we describe the first analysis of serpentine by atom probe tomography (APT). This technique is fairly new to planetary science, but is potentially extremely powerful as it can reveal the chemical and isotopic compositions and nanostructure of samples ~ 0.01  $\mu\text{m}^3$  in size and in three dimensions (Miller and Russell 1992, Kelly and Larson 2012, Valley *et al.* 2014, Heck *et al.* 2014, Daly *et al.* 2017, 2018, 2020, White *et al.* 2017, 2020, Saxey *et al.* 2018, Fougereuse *et al.* 2020, Greer *et al.* 2020, Reddy *et al.* 2020). This nanoscale information is crucial to understanding early solar system processes (e.g., water-rock reactions in primitive asteroids (White *et al.* 2020) and in Martian meteorites (Daly *et al.* 2020)). However, it has not thus far been possible to routinely measure phyllosilicates especially clays and other hydrous phases by APT as this type of analysis is even more challenging than conventional techniques, only lithium-bearing mica has been measured by APT thus far (Reddy *et al.* 2020). Here we have developed and tested protocols for analysing serpentine by APT for the first time in order to improve the methodology for minerals analogous to those that will be returned from Ryugu and Bennu.

## Materials and methods

This study used serpentine from the Ronda peridotite (RP), which crops out over ~ 450 km<sup>2</sup> in the Betic Cordillera of southern Spain (Figure 1). In addition to phyllosilicate, the peridotite contains olivine, orthopyroxene and clinopyroxene, often accompanied by minor garnet and/or plagioclase feldspar (Obata *et al.* 1980). Serpentinisation took

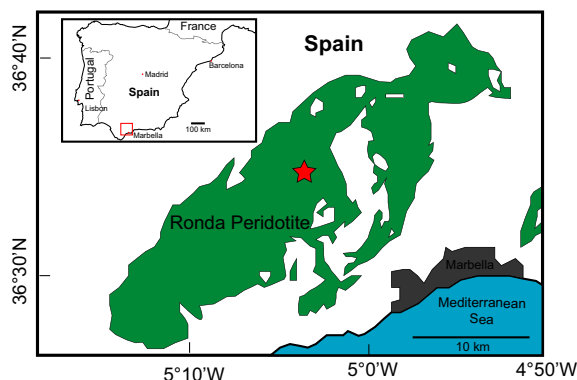


**Figure 1. Geological map of the Ronda peridotite (green) outcrop in southern Spain. The star indicates where the sample for this study was collected. Adapted from Etiope *et al.* (2016).**

place in the upper continental crust ( $< 4$  kbar), 19–22 My ago (Pedrera *et al.* 2016). Samples for this study were retrieved from the plagioclase tectonite domain, the youngest of three tectonometamorphic domains described by Wal and Vissers (1996) and otherwise known as the plagioclase lherzolite domain (Obata *et al.* 1980). This unit comprises porphyroclastic plagioclase peridotites, subordinate mylonites and layers of spinel–plagioclase–websterites. The original magmatic and deformation structures in this domain have been completely overprinted with textures related to its crustal emplacement. Samples were collected from this plagioclase peridotite exposed on the east side of the A-397, 18 km northwest of Marbella ( $36^{\circ}35'06.8''\text{N}$   $5^{\circ}04'09.8''\text{W}$ ) (Figure 1).

Ronda peridotite samples were made into polished thin sections, coated with  $\sim 5$  nm of carbon, and characterised at the University of Glasgow (UoG) using a Zeiss Sigma variable pressure field-emission SEM that is equipped with an Oxford Instruments X-Max 80  $\text{mm}^2$  silicon drift energy-dispersive X-ray (EDX) detector. SEM was used for backscattered electron (BSE) imaging and quantitative chemical analysis by energy-dispersive X-ray spectrometry (EDS; Table 1; Figures 2 and 3; Table S3). For chemical analyses, the beam was rastered over a  $\sim 50 \times 50 \mu\text{m}$  area for 60 s using a beam current of 1 nA. Beam currents were measured using a Faraday cup. Spectra were quantified using mineral reference materials: periclase (Mg), diopside (Al and Si) and garnet (Fe). The water content of phyllosilicates was approximated from the EDS data by assuming that the difference in analytical totals from 100% *m/m* was due to unanalysed water. However, the presence of porosity and other unstandardised elements (e.g., Mn) will contribute to an overestimation of water contents.

Electron-transparent samples of the serpentine were prepared and studied by TEM at the UoG. Samples were prepared using a focused ion beam (FIB). The region to be extracted for TEM was initially protected from damage from the ion beam and electron beam during sample preparation by depositing a  $1 \mu\text{m}$  thick layer of Pt using the gas injection system. Lamellae  $\sim 100$  nm in thickness were extracted from serpentine veins in the polished thin section, with the midplane of the lamellae oriented normal to the long axes of the veins and approximately parallel to the cleavage of the serpentine. A FEI Nova NanoLab 200 dual-beam  $\text{Ga}^+$  FIB was used, operated at 30 kV and using a range of beam currents as well as a final 5 kV polish and minimised SEM imaging of the sample surface; this approach is outlined by Lee *et al.* (2003) and results in minimum ion beam damage of the resulting sample. Diffraction-contrast and high-resolution images of the

lamellae were obtained using a FEI T20 TEM operated at 200 kV (Figure 2). TEM data were collected rapidly, exposing the sample for the minimum amount of time (few seconds) to minimise beam damage to the sample (Lee *et al.* 2015a, b, Lee and Smith, 2006, Lee *et al.* 2007a, b, Utsunomiya *et al.* 2009). Ten APT specimens were extracted from two serpentine veins in the polished thin section (five APT samples from each, Figure 3) with their long axes oriented normal to the long axes of the veins and parallel to the cleavage of the serpentine following the approach of (Thompson *et al.* 2007). As with the TEM samples, a protective  $1 \mu\text{m}$  thick bar of platinum was deposited over the region of interest using a GIS to protect it from beam damage (Thompson *et al.* 2007). These specimens were attached to an electropolished molybdenum half grid using the Thermo Scientific Helios G4 Plasma FIB-SEM in the Australian Centre for Microscopy and Microanalysis at the University of Sydney (ACMM, USyd) that was operated using a Xe ion beam which was chosen for its higher milling rates and lower beam damage than Ga-based FIBs. The samples were then thinned to a needle-like shape via an annular milling pattern followed by a final low kV polish to remove any remnants of the Pt cap and  $\sim 1 \mu\text{m}$  from the top of the serpentine to remove the damage induced into the sample from SEM pre-characterisation and the damage layer induced by previous annular milling thus minimising ion implantation and volatile loss from the sample using a Zeiss Auriga Ga-FIB-SEM at USyd following typical FIB-based APT sample preparation protocols (Thompson *et al.* 2007). Samples were transferred directly from the FIB to the APT or, where this was not possible, they were stored at atmospheric pressure in a desiccator for a few days to a week.

The APT samples were analysed on the CAMECA LEAP 4000X HR Si atom probe at the ACMM. The analytical conditions for the larger data sets are outlined in Table S1 while the smaller data sets are outlined in Table S2. The serpentine began to field evaporate at very low voltages ( $\sim 500$  V). During APT analyses, which ran to  $> 5$  million ion data sets, APT laser energy was varied to establish the effect of analytical parameters (Figure S1). The automated focus of the laser in the *x*, *y* and *z* directions was disabled and positioned manually as the automated laser focus migrated down the shank of the needle, eventually focussing on the Pt weld, leading to premature sample fracture. The laser focus operates by identifying the location of highest detection events, normally occurring at the tip apex where the field is strongest, though in the case of the sample tips in this study, the highest detection events occurred when the laser was focused on the shank of the tip. The data were reconstructed and investigated using the IVAS software from CAMECA.

Because of this manual focus and the sporadic voltage curve (Figure S1), the resulting universal atomic mass unit/charge state ( $u/q$ ) spectrum exhibited broad multi-peak curves for

each isotope of each element (Figure S2A, B). Each data set was further reconstructed into segments of common analytical conditions, that is laser power to assess the effect of these

**Table 1.**  
**EDS and APT geochemical measurement results (in atomic %)**

Mineral	EDS				Fe	Mg#	Water*
	Mg	Si	O	Al			
Olivine	25.47	14.54	57.28	0.05	2.67	0.91	n/a
Olivine	25.49	14.55	57.29	0.07	2.60	0.91	n/a
Olivine	25.52	14.51	57.26	0.07	2.63	0.91	n/a
Olivine	25.49	14.53	57.27	0.05	2.65	0.91	n/a
Olivine	25.38	14.55	57.29	0.07	2.72	0.90	n/a
Olivine	25.49	14.52	57.27	0.06	2.67	0.91	n/a
Olivine	25.39	14.52	57.28	0.12	2.69	0.90	n/a
Olivine	25.44	14.45	57.24	0.06	2.81	0.90	n/a
Olivine	25.55	14.49	57.25	0.06	2.64	0.91	n/a
Olivine	25.07	14.70	57.36	0.08	2.79	0.90	n/a
Olivine	24.81	15.02	57.56	0.23	2.37	0.91	n/a
Serpentine	18.47	13.92	47.14	0.00	0.94	0.95	19.53
Serpentine	18.67	14.03	48.16	0.05	1.38	0.93	17.72
Serpentine	19.39	14.47	49.70	0.08	1.25	0.94	15.11
Serpentine	19.18	14.32	49.25	0.04	1.39	0.93	15.82
Serpentine	18.69	12.61	45.53	0.04	1.57	0.92	21.56
Serpentine	18.84	13.88	47.78	0.07	1.08	0.95	18.35
Serpentine	18.70	12.71	45.74	0.02	1.61	0.92	21.23
Serpentine	18.02	12.78	45.55	0.05	1.90	0.90	21.70
Serpentine	17.55	12.97	45.34	0.06	1.78	0.91	22.30
Serpentine	18.33	13.20	46.75	0.42	1.41	0.93	19.89
Serpentine	18.74	14.26	48.50	0.07	1.15	0.94	17.28
Serpentine	18.68	13.39	47.18	0.07	1.62	0.92	19.06
Serpentine	19.01	13.12	46.97	0.06	1.65	0.92	19.20
Serpentine	19.33	14.01	48.52	0.05	1.11	0.95	16.98
Serpentine	18.34	13.55	47.08	0.07	1.54	0.92	19.41
Serpentine	18.68	13.92	47.63	0.02	1.10	0.94	18.65
Serpentine	19.07	14.45	49.08	0.02	1.09	0.95	16.29
Serpentine	19.53	14.21	49.09	0.08	1.02	0.95	16.06
Serpentine	19.02	13.33	47.26	0.05	1.51	0.93	18.83

Mineral	APT					Mg#	Water**	H***	laser energy	APT Sample
	Mg	Si	O	Al	Fe					
Serpentine	31.80	13.31	45.76	0.08	0.18	0.99	7.92	8.36	100 $\mu$ J	RP1
Serpentine	32.64	13.40	48.45	0.20	0.14	1.00	4.50	5.06	200 $\mu$ J	RP1
Serpentine	34.69	13.15	41.57	0.03	0.08	1.00	6.06	10.48	all	RP1
Serpentine	29.46	14.35	49.45	0.08	0.06	1.00	5.66	6.32	20 $\mu$ J	RP2
Serpentine	30.52	16.21	46.32	0.11	0.07	1.00	1.63	5.82	50 $\mu$ J	RP2
Serpentine	28.89	14.10	51.10	0.18	0.18	0.99	3.04	4.31	100 $\mu$ J	RP2
Serpentine	31.93	12.24	50.44	0.03	0.00	1.00	1.67	3.66	all	RP2
SiO-rich	1.07	32.84	59.10	0.06	0.00	1.00	6.06	6.94	100 $\mu$ J	RP1
SiO-rich	1.67	29.56	64.59	0.00	0.00	1.00	2.54	3.14	200 $\mu$ J	RP1
SiO-rich	3.61	21.63	64.59	0.00	0.02	0.99	5.75	9.86	all	RP1
SiO-rich	1.79	29.91	59.90	0.02	0.12	0.94	10.72	8.17	20 $\mu$ J	RP2
SiO-rich	2.39	35.33	50.89	0.10	0.00	1.00	6.42	2.41	50 $\mu$ J	RP2
SiO-rich	2.14	31.36	61.14	0.00	0.09	0.96	3.80	5.06	100 $\mu$ J	RP2
SiO-rich	2.30	28.52	62.92	0.02	0.00	1.00	6.07	6.20	all	RP2
Bulk needle	31.78	13.34	46.67	0.10	0.17	0.99	7.00	7.51	100 $\mu$ J	RP1
Bulk needle	33.43	12.45	48.52	0.14	0.09	1.00	4.67	5.27	200 $\mu$ J	RP1
Bulk needle	33.79	12.95	42.48	0.03	0.09	1.00	6.30	10.66	all	RP1
Bulk needle	27.79	15.22	50.07	0.07	0.06	1.00	5.85	6.57	20 $\mu$ J	RP2
Bulk needle	29.51	16.55	44.83	0.13	0.07	1.00	4.11	7.58	50 $\mu$ J	RP2

**Table 1 (continued).**  
**EDS and APT geochemical measurement results (in atomic %)**

Mineral	APT					Mg#	Water**	H***	laser energy	APT Sample
	Mg	Si	O	Al	Fe					
Bulk needle	25.65	16.16	52.81	0.12	0.18	0.99	2.78	5.02	100 $\mu$ J	RP2
Bulk needle	30.54	12.13	52.77	0.03	0.06	1.00	0.86	3.18	all	RP2

EDS measurement results are of the bulk olivine and serpentine. APT measurement results are split into each dataset as a whole, separating SiO and Mg rich (RP) regions, as well as segmenting the data by laser power. Atomic % water of APT data content was calculated by adding H<sub>2</sub>O, OH and H<sub>3</sub>O ionic fractions. Atomic % H of APT data was calculated by adding all species with H ions including H<sub>2</sub>O, OH and H<sub>3</sub>O.

\* Calculated assuming the low EDS totals reflect the presence of H<sub>2</sub>O within the sample.

\*\* Sum of *u/q* spectra 17 (OH), 18 (H<sub>2</sub>O), and 19 (H<sub>3</sub>O) peaks and assuming OH<sup>+</sup> bound in the serpentine structure is equivalent to water when released.

\*\*\* Sum of all H<sup>+</sup> bearing ion species ion counts identified in *u/q* spectra including those from OH<sup>+</sup>, H<sub>2</sub>O<sup>+</sup> and H<sub>3</sub>O<sup>+</sup>.

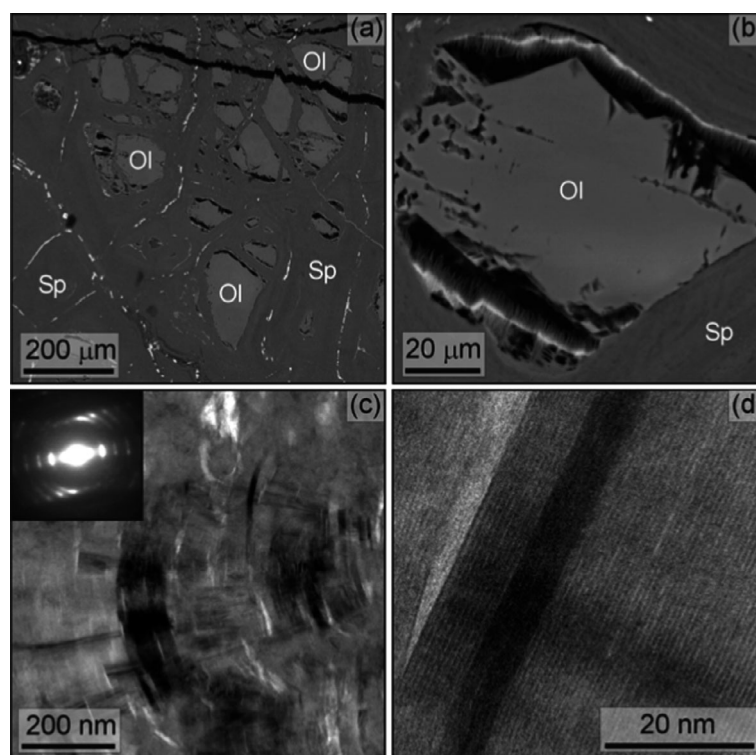


**Figure 2.** Images of the RP. (a) BSE image showing the domains of olivine (Ol) enclosed within serpentine (Sp). Axial selvages of iron oxide are white. (b) BSE image of a domain of olivine (Ol) that contains lines of etch pits with planar and sawtooth edges. The surrounding serpentine (Sp) is finely laminated. (c) Bright-field TEM image of serpentine showing that it is made of bunched layer packets that are a few tens of nm in thickness. A SAED pattern is inset. The basal layer d-spacing is 0.73 nm, which is consistent with lizardite (001). (d) High-resolution TEM image of the phyllosilicate showing ~ 0.73 nm fringes of serpentine (001) planes.

settings on the resultant data set while also improving the mass spectra mitigating the ‘foresting’ effect and thus aiding identification of mass peaks derived from each element and isotope (Figure S2C, D). In addition, sections of each APT data set representative of each laser energy were reconstructed separately to evaluate the effect of varying laser

power (Figure S2C, D). The counts under each peak in the *u/q* spectrum for each data set were ranged using the IVAS software and using the full width of the peak and assigned as an elemental ion or molecular ion to determine bulk composition. The presence of two discrete domains (serpentine matrix and SiO-rich nanophase) was revealed by



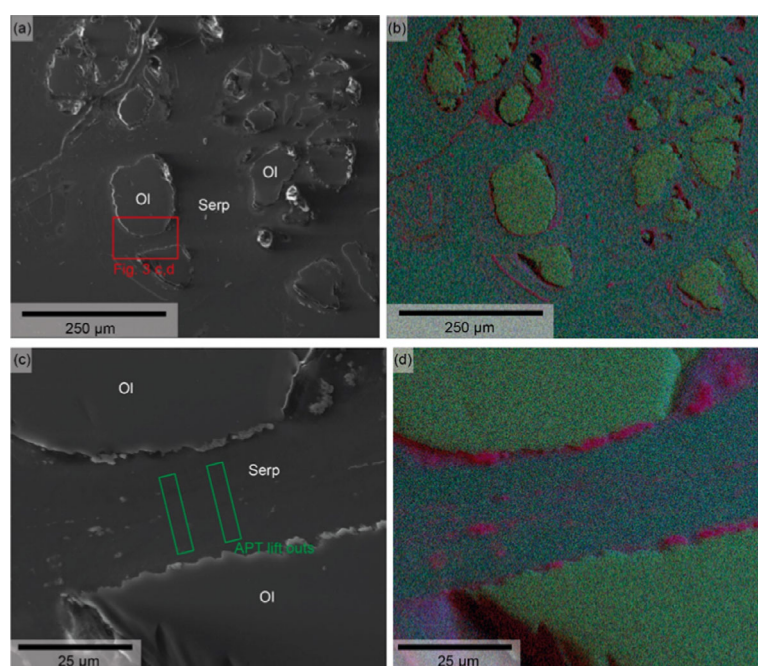


**Figure 3.** (a, c) Secondary electron images and (b, d) false colour red (Fe), green (Mg) blue (Si) EDS map of Ronda peridotite at two magnifications. The green boxes indicate where atom probe samples were extracted by focused ion beam from the serpentine.

generating iso-concentration surfaces defined by Mg concentration of 8–12 at. % (Figure 4). The compositional change across the interface of these two phases was established by generating a proximity histogram (proxigram) with a bin width of 0.2 nm (Hellman *et al.* 2000, Figure 4). The composition of these discrete phases was established by reconstructing the data sets from the higher (serpentine) and lower (SiO-rich) gradient side of the Mg isosurface and ranging the  $u/q$  spectrum peaks for each phase in the same way as described here (Table 1; Figure S2E–H). The water content of the APT data is calculated from the sum of the APT  $u/q$  spectra peaks at 17 ( $\text{OH}^+$ ), 18 ( $\text{H}_2\text{O}^+$ ) and 19 ( $\text{H}_3\text{O}^+$ ). The contributions of isotopes of  $\text{O}^+$  to these  $u/q$  peaks is considered negligible as these peaks are substantially larger (three and two orders of magnitude) than expected terrestrial O isotope abundances for  $^{17}\text{O}$  and  $^{18}\text{O}$ , respectively, while major S contributions can be ruled out as no  $^{33}\text{S}^{2+}$  peak is observed at 16.5  $u/q$ . APT measurements also contain hydrogen and hydroxyl species derived from the absorption of hydrogen onto the APT needle in the ultra-high vacuum, which is exacerbated by the cryogenically cooled APT needle. However, typical background hydrogen for geological APT data sets is < 1 at. % (Pérez-Huerta *et al.* 2016, Greer *et al.* 2020) and is predominantly present in the 1 and 2  $u/q$  peaks of the mass spectra (Table 1). We are thus confident that water abundance calculated by APT is a real water signal, indigenous to the sample because it is

substantially in excess (~ 6 at. % on average) of typical APT background hydrogen (1 at. %) detected in similar materials, and we do not include the 1 and 2  $u/q$  peaks that represent  $\text{H}^+$  and  $\text{H}_2^+$  in our quantification (Table 1). To account for the ‘worst case scenario’ of water contamination from instrument effects in our APT, data 1 at. % could be subtracted from our calculated water abundance to provide a minimum indigenous water content of our samples of ~ 5 at. % on average. In addition, serpentine group minerals are hydrated and typically comprise up to 13%  $m/m$  water (Schwartz *et al.* 2013), and as such, elevated water abundances are to be expected in APT measurements.

## Results

### Petrography, microstructure and chemical composition

The Ronda samples are petrographically comparable to a partially serpentinised peridotite (i.e., some of the original olivine mineralogy remains, Figure 2a). They have a characteristic mesh texture comprising serpentine veins up to ~ 1 mm in width that enclose and cross-cut sub-mm size domains of olivine (Figure 2a). Domains have planar or sawtooth edges and the olivine contains etch pits (Figure 2b). BSE images show that the serpentine has a fine-scale layering (~ 5–10  $\mu\text{m}$ ) and contains iron oxides

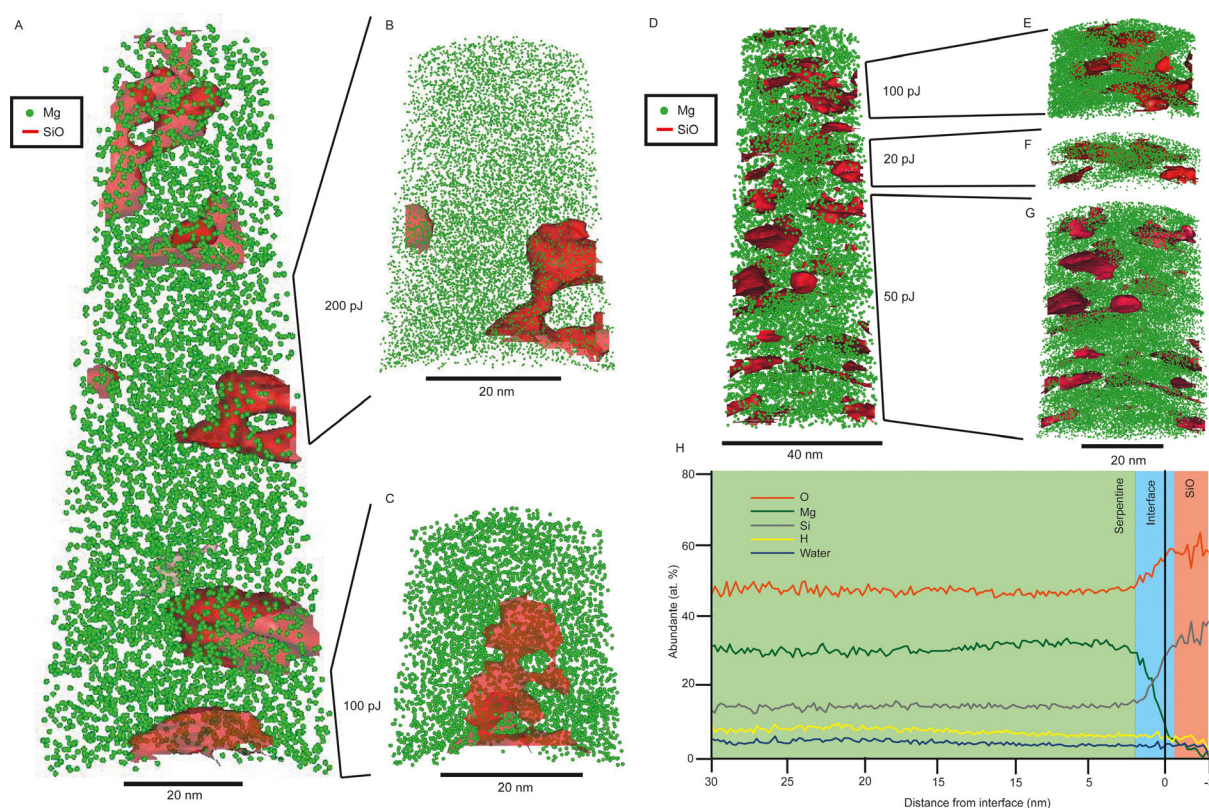


**Figure 4.** Atom probe reconstructions of RP 1 (a–c) and RP 2 (d–g) of both the entire analysed volume (a, d) and discrete representative portions where a consistent laser energy was used. Magnesium spheres highlight the distribution of the serpentine phase. The red isosurfaces represent the extent of the SiO-rich nanophase within which the concentration of Mg is less than 8–12 at. %. (h) Geochemical concentration profiles between the SiO-rich volume and Mg-rich volume in RP2 (d). The interface is sharp over 2 nm.

(haematite or magnetite) that are finely disseminated through the veins and are also concentrated as selvages along vein axes (Figure 2a, b).

The olivine is compositionally close to end-member forsterite (Mg# 0.91; Table 1, Figure 3b), and vein analyses have a stoichiometry that is consistent with serpentine (i.e., mean atomic (Mg + Fe)/Si = 1.5). The Mg-rich composition of this serpentine (Mg# 0.93) is indicative of chrysotile or lizardite; the latter is the most likely as it is the dominant phyllosilicate in the Ronda peridotites (Esteban *et al.* 2003) (Table 1). The mean analytical total by quantitative EDS of the serpentine (83.3% *m/m*) suggests that it has 16.7% *m/m* of undetected material, presumed to be primarily the low atomic number (light) elements of water, although this value is likely to be an overestimate owing to the presence of porosity and other unstandardised and low atomic number elements.

TEM images show that the phyllosilicate veins are comprised of crystallites that differ slightly in orientation and are a few tens of nanometres thick parallel to their *c*-axes

(Figure 2c). Lattice fringe images and SAED patterns show that these crystals have the ~ 0.75 nm basal spacing that is consistent with lizardite (Figure 2d).

Measurements of the mean composition of the phyllosilicate as derived from APT are broadly in agreement with the EDS data, although with lower Fe, Si and hydroxyl contents and higher Mg (Table 1). The water content detected in APT data is reduced in regions where the laser energy was higher, but otherwise laser energy had no systematic effect on the bulk chemistry (Table 1). The phyllosilicate layering structure observed in TEM is not seen in the APT point clouds because they are chemically homogeneous (i.e., TEM reveals crystallographic nanostructures, whereas APT reveals chemical nanostructures). However, APT shows that the serpentine veins contain rounded nanophases 2–20 nm in size. They have a very low density of atoms relative to the surrounding phyllosilicates and are depleted in Mg and enriched in Si and O relative to the serpentine such that they are close to stoichiometric SiO<sub>2</sub> in composition (Table 1; Figure 4). The bases of these SiO-rich nanophases are planar, but this is

likely an analysis artefact due to the evaporation of the remaining portion of each inclusion in a large burst and as such is not the true geometry of these nanophases. Chemical profiles between the SiO-rich phase and lizardite reveal that the boundary is sharp over 1–2 nm (Figure 4h) and the lizardite and SiO-rich volumes are compositionally homogeneous. Nanophase-like artefacts can be produced in APT data as a result of surface diffusion of ions resulting in preferential evaporation from hotspots. However, such hotspots tend to increase the density of ions present which is not observed here and these structures remain across a variety of laser energies and have a sharp compositional boundary providing further evidence that these nanophase SiO-rich volumes are real features of sample.

Removing SiO-rich volumes from the  $u/q$  spectrum analysis reveal that while small and SiO rich, their low density of ions results in an underestimation of O and Si in the bulk APT sample relative to pure lizardite measured by EDS by 1–2 at. % (Table 1). The SiO nanophases were not detected by high-resolution TEM (HR-TEM) imaging or electron diffraction. The absence of clear SiO nanophase morphologies in HR-TEM images may be due to the thickness of the TEM lamellae (100 nm) relative to the SiO nanophases (2–20 nm), while the absence of spot diffraction patterns of a crystalline SiO phase alongside the lizardite suggests that if SiO nanophases are present in the TEM lamellae they are amorphous (Figure 2c, d).

## Discussion

We first describe the effectiveness of the approaches that we tested for analysis of phyllosilicates by APT and propose protocols for future work. We then discuss the implications of our results for understanding the formation of Ronda lizardite and peridotite serpentinisation more broadly. Finally, we consider the implications of this work for studying and understanding samples that will be returned from Ryugu, Bennu and Mars.

### APT analysis of phyllosilicates

APT could be a powerful tool in understanding the chemical, isotopic and nanostructures and even water content of delicate materials, such as clays, providing information that cannot be gleaned from other techniques. However, analysing hydrous clay phases is incredibly challenging due to the volatility of water and the sensitivity of the mineral to alteration during sample preparation, storage and analysis. This study shows that it is indeed possible to analyse such materials by APT. All of the APT tips provided some data. Eight tips yielded a few hundred

thousand atoms and two tips yielded > 1 million ion data sets (RP 1 and RP 2). With one exception (RP1), all samples fractured once the voltage had exceeded 3000–4000 V, suggesting that, for the most part, serpentine is structurally weak and unable to withstand high field strengths. In addition, samples that were analysed soon after FIB preparation were most likely to yield large data sets, while those that were analysed days to weeks after they have been prepared, despite storage in a desiccator, did not run well, particularly those left at atmospheric pressure. This may be due to adsorption or desorption of water in the phyllosilicate causing expansion and contraction of the specimen, weakening the structure and/or bond with the substrate. In addition, samples with a greater distance between the apex of the tip and the Pt weld and samples with a larger apex diameter and large shank angle seemed to run for greater lengths of time which may be a result of the greater structural integrity provided by the thicker apex and wider shank angle, although a small sample set means that these observations are anecdotal and not statistical. Varying the laser power seems to have minimal effect on the voltage, the susceptibility of the sample to fracture or the  $u/q$  spectra of serpentine (Tables 1, S1 and S2; Figures S1 and S2); however, an increase in laser power results in a reduction in the total water content detected by APT. This water reduction with increase in laser power is likely due to thermal heating of the sample by the laser resulting in evaporation of the water but otherwise has no systematic effect on the bulk chemistry (Table 1). Based on these findings, we recommend the following analytical pipeline for APT analysis of serpentine and other phyllosilicate minerals, after preliminary characterisation of the region of interest by Raman spectroscopy, cathodoluminescence and EDS to establish mineralogy to aid APT data interpretation, and where the APT needle is extracted parallel to the cleavage of the mineral.

- (1) The APT sample geometry for serpentine should situate the apex of the sample as far from the Pt deposition as possible (> 5  $\mu\text{m}$ ) to avoid the APT laser encompassing, or focussing on, the weld region. If the tip apex is too close to the Pt deposition, it is thought that the difference in the field of evaporation between the sample and the Pt leads to field evaporation of the deposition, rather than the sample, resulting in fracture. We recommend manual x-y-z focusing of the laser should be employed to keep focus on the apex of the tip and to avoid migration of the laser down the shank that was observed in automated laser positioning.
- (2) The initial APT sample diameter prepared by FIB should be larger ( $\sim 150$  nm) than typical APT specimens ( $\leq \sim 100$  nm) and should be prepared



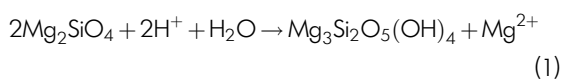
with a larger shank angle ( $\sim 10^\circ$ ) than is typical for APT specimens, to increase the structural integrity of the tip and decrease the likelihood of sample failure; however, this will result in an overall increase of the voltage required for field evaporation.

- (3) Samples should be transferred directly from the FIB vacuum to the APT to minimise time at ambient humidity and temperature.
- (4) APT settings should be optimised to collect as much data as possible at below  $\sim 4000$  V to avoid sample fracture, while laser energy should initially be set as low as possible to avoid water loss from the sample due to thermal heating. Thus, during any given analysis, the laser energy should increase during the analysis up to ( $\sim 100$ – $200$  pJ) in order to minimise water loss while keeping the voltage below  $4000$  V, which despite RP 1 continuing to provide data above  $4000$  V, appears to be a structural limit for the majority of these samples.

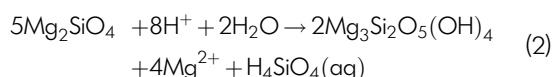
It should be noted that recommendations 2 and 4 could be perceived as conflicting and reflect a compromise that should be considered during sample fabrication.

### Serpentinisation of the Ronda peridotite

The mesh texture of the Ronda samples is characteristic of the replacement of olivine by serpentine (Figure 2a, b). Serpentinisation can be described by a variety of reactions, as outlined by Velbel (2014). For example, in reaction (1), all Si liberated from olivine is retained in lizardite but some of the Mg is leached from the area and transported elsewhere by the fluid, and as a consequence, solid volume increases by 23%:



By contrast, reaction (2) is almost isovolumetric ( $< 2\%$  volume decrease) and only a proportion of the Mg and Si liberated from olivine goes into the lizardite:



These reactions are a simplification because Ronda olivine contains  $\sim 9\%$  *m/m* FeO. The occurrence of iron oxides within the veins suggests that some of the iron that was liberated from olivine during serpentinisation was oxidised. Thus, only a proportion of the iron measured by EDS analyses of the veins is in the serpentine. Lizardite is likely

to be closer to end-member Mg-serpentine than indicated by its EDS-determined Mg# of 0.93. The presence of separate SiO-rich nanodomains within the lizardite APT data suggests that in the case of the Ronda peridotite reaction (2) was dominant and that the excess Mg produced by the reaction is not present in the APT volume analysed.

### Nanoscale chemistry and microstructure of the serpentine veins

At the resolution of SEM and TEM observations, the Ronda samples are microstructurally and compositionally typical of a serpentinised peridotite. The APT data, however, reveal a new level of nanoscale information. Chemical compositions of the veins as measured by EDS and APT are consistent with a Mg-serpentine. However, Fe concentrations are higher in the EDS than APT data, which is in part due to the much greater interaction volume that would have included disseminated Fe-oxides that are absent from the APT data sets [i.e., analytical volumes were  $\sim 35 \mu\text{m}^3$  by EDS vs.  $\sim 0.01 \mu\text{m}^3$  for a whole APT needle (Fougerouse *et al.* 2020)]. This explanation is also consistent with the fact that the Fe peaks in the *u/q* spectra were small but resolvable (Figure S2).

The atomic (Mg + Fe)/Si ratio of lizardite measured by EDS (mean 1.5) is lower than the APT analyses of serpentine (mean 2.3) and bulk needle data (mean 2.2; Table 1). This is likely due to a combination of factors. Firstly, the EDS interaction volume may have incorporated some Fe oxides while the APT data only measured lizardite. Secondly, the Si and O ions from the SiO-rich nanophases are underrepresented owing to their significantly lower ion density than the surrounding serpentine. This factor, coupled with the tendency of the SiO-rich domains to be plucked off during APT analysis (as evidenced by their flat bases, Figure 3), suggests that the SiO phase was ionised less readily than lizardite at the voltages and laser energies where lizardite began to field evaporate. As a consequence, fewer ions and volumes were extracted from SiO nanospheres than from the lizardite during APT analysis. This results in a local magnification effect (Vurpillot *et al.* 2000, Fougerouse *et al.* 2016) as the difference in field between the phases would result in a skewed chemical quantification and 3D reconstruction (Vurpillot *et al.* 2000, Fougerouse *et al.* 2016). Thus, the Mg/Si ratios of bulk needles ( $\sim 2.2$ ) are higher than expected given the observed volume of nanospheres and are close to the Mg/Si ratios of pure lizardite as measured by APT ( $\sim 2.3$ ). If atoms had been extracted from the SiO nanospheres with the same efficiency as from the lizardite, Mg/Si ratios of the bulk needles would have been lower than the Mg/Si ratio of pure lizardite as measured by APT

and closer to the ratio measured by EDS ( $\sim 1.5$ ). This magnification effect would also explain the slightly diffuse boundary  $\sim 2$  nm between the SiO-rich domain and the matrix (Figure 4; Vurpillot *et al.* 2000, Fougereuse *et al.* 2016).

The water content of the lizardite as inferred from EDS analytical totals (16.7% *m/m*) is higher than stoichiometric lizardite (13.0% *m/m*), which is probably due to the presence of porosity and unquantified elements. Water contents from EDS are also significantly higher than estimated from APT data ( $\sim 18.7$  vs.  $\sim 6.5$  at. %, respectively) even taking into account the overestimation of  $\sim 3.7\%$  *m/m*. Thus, water contents measured by APT are underestimated by several at. %, which could be caused by a number of factors. Firstly, this water content could be caused by hydroxyl ions generated during atom probe analysis by absorption of hydrogen gas in the ultra-high vacuum chamber of the atom probe onto the APT specimen. However, as discussed previously, our APT water measurements are substantially greater than typical background H measurements ( $< 1$  at. %) in APT (Pérez-Huerta *et al.* 2016, Greer *et al.* 2020). The signal of the 17 *u/q* and 18 *u/q* peaks in the Ronda mass spectra are also far higher than natural O isotope abundances (two orders of magnitude, Figure S2) suggesting that the water measurements in our data are above and beyond typical APT H instrumentation effects. As such, the majority of the hydroxyl ions detected are likely to be indigenous to the sample but are still less abundant than expected for lizardite. Some water, particularly free water present between the crystal lattices, will likely have been lost by evaporation during FIB sample preparation, through exposure to the ultra-high vacuum of the APT sample chamber, or as a consequence of heating by the ultraviolet laser that lowered the total hydroxyl ion signal. However, it is also possible that the lower than expected water content could reflect intrinsic properties of the samples. For example, the phyllosilicates may not have been solely lizardite and included intergrowths of antigorite. This mineral has a lower water content than lizardite (Malpas 1992) and is common in the RP (Pedrera *et al.* 2016).

A notable feature of the APT data sets is the SiO nanodomains, highlighting the value of 3D chemical analysis over the depth (100 nm) of a typical TEM sample. The SiO nanodomains are not visible in the TEM diffraction-contrast and lattice fringe images (Figure 2d), which may be due to their heterogeneous distribution (the TEM and APT samples were cut from different veins) but is more likely because they are made of amorphous opaline silica. Silica-rich phases including quartz are very rare in serpentinites (Frost and Beard 2007) and so the nano-inclusions are

unexpected. We suggest that they have formed by isovolumetric serpentinisation, as described in reaction (2), a by-product of which is orthosilicic acid. Nanodomains of opal-A (amorphous  $\text{SiO}_2 \cdot n\text{H}_2\text{O}$ )  $\sim 12$  nm in diameter have also been identified in the Martian meteorite Nakhla by TEM-EDS (Lee *et al.* 2015b). The nanospheres occur within olivine-hosted veins of iddingsite, which is a very fine-scale intergrowth of ferrihydrite with nontronite that formed by the water-mediated alteration of olivine the shallow crust of Mars (Bunch and Reid 1975, Lee *et al.* 2015a). Silica nano-inclusions in intimate association with phyllosilicates may be a common by-product of the water-mediated alteration of olivine. This work therefore shows that APT is a powerful tool for extracting robust geochemical information from specific phases even within nanophase assemblages such as those of the RP serpentine.

### Using APT to study samples returned from asteroids and from Mars

Approximately 60 g or 100 mg of sample, at most, will be returned from Bennu and Ryugu, respectively (Tsuda *et al.* 2013, Lauretta *et al.* 2017, Sawada *et al.* 2017). If these two asteroids are mineralogically similar to the CMs as predicted (Lauretta *et al.* 2015, Perna *et al.* 2017, Bates *et al.* 2020), the majority of the returned material will comprise serpentine, which constitutes 56–91 vol. % of the CMs (Howard *et al.* 2015, King *et al.* 2017, Lee *et al.* 2019a, b). As APT yields a wealth of information on the chemistry and nanostructure of serpentine, while destroying very little material ( $\sim 0.01 \mu\text{m}^3$  per needle during APT analysis;  $\sim 400 \mu\text{m}^3$ /FIB-lift out APT sample fabrication for  $\sim 10$  APT needles), this study shows that APT is suitable as a front-line technique to analyse Ryugu and Bennu samples. In the long term, phyllosilicate minerals are a prime target for the eventual Mars Sample Return mission (iMOST 2018) so the results of this study will be directly applicable for returned Martian samples as well (Daly *et al.* 2020).

APT has the potential to answer some of the key questions being asked of these two asteroids. For example, the chemical composition of the serpentine can reveal the extent to which the constituent rocks have reacted with liquid water because the proportion of Mg- to Fe-rich serpentine increases with the degree of water/rock interaction (Browning *et al.* 1996, Howard *et al.* 2015). The unexpected presence of silica nanoparticles may be explained because Velbel (2014) concluded that reaction (2) best describes the serpentinisation of olivine in the CMs. APT can also be used to answer the question of whether the asteroidal phyllosilicates have been thermally dehydroxylated, as suggested for Ryugu (Kitazato *et al.* 2019), by measuring OH and  $\text{H}_2\text{O}$

concentrations and how they differ between samples and within specific nanoscale domains and phases. If the lower water content of lizardite APT samples (Table 1) relative to typical lizardite minerals is an indigenous signal of the samples, then APT could be used as a new tool to detect evidence for dehydroxylation reactions and low-temperature thermal metamorphism of serpentines including those in CM chondrites. The use of cryo-FIB to cryo-transfer techniques to prepare phyllosilicate samples in the future should evaluate if FIB preparation results in any substantial volatile loss from the specimen and so answer these questions more conclusively.

## Conclusions

Results from the present study highlight the effectiveness of APT for characterising phyllosilicates, which will be key minerals to identify, given that they fingerprint the former presence of liquid water. This study also demonstrates that this approach could be applied more broadly to other hydrous mineralogies.

APT analysis of phyllosilicates here reveal new SiO-rich nanophases that provide new insights into the nature of the fluid and reaction pathway that was dominant during serpentinisation of the Ronda peridotite, and we predict that similar nanophases may be a common by-product of serpentinisation, that can only be detected by APT. Serpentine group minerals may be present in the returned samples from C-type asteroids Ryugu and Bennu, and eventually from Mars, as it occurs in meteorites that have been impact-ejected from the shallow crust and at the surface of Mars (Treiman and Gooding 1991, Imae and Ikeda 2007, Ehlmann *et al.* 2010). As such, APT has the potential to be a key tool for the analysis of planetary samples including those that will be returned from the hydrous asteroids Ryugu and Bennu in the near term and eventually from Mars within the next 10–15 years (Daly *et al.* 2020).

## Acknowledgements

This work was funded by STFC grant ST/T002328/1 awarded to M.R.L., J.D. and L.D. and the Glasgow-Sydney Partnership Collaboration Award awarded to J.C. and M.R.L. The authors acknowledge the instruments and scientific and technical assistance of Microscopy Australia at the Australian Centre for Microscopy and Microanalysis, the University of Sydney, the ISAAC electron microscopy facility at the University of Glasgow especially technical assistance from Mr. P. Chung, and the Atom probe facility at the University of Oxford. This work was also conducted within the Geoscience Atom Probe Facility at Curtin University, which is part of the

Advanced Resource Characterisation Facility (ARCF). The Advanced Resource Characterisation Facility is being developed under the auspices of the National Resource Sciences Precinct – a collaboration between CSIRO, Curtin University and The University of Western Australia – and is supported by the Science and Industry Endowment Fund. The authors would also like to thank Editor Regina Mertz-Kraus and two anonymous reviewers for their detailed comments and suggestions that improved the manuscript.

## Data availability statement

The data that support the findings of this study are available in the supplementary material of this article.

## References

- Banin A. and Margulies L. (1983)**  
Simulation of Viking biology experiments suggest smectites not palagonites, as Martian soil analogues. *Nature*, **305**, 523–525.
- Barber D.J. (1981)**  
Matrix phyllosilicates and associated minerals in C2M carbonaceous chondrites. *Geochimica et Cosmochimica Acta*, **45**, 945–970.
- Bates H.C., King A.J., Donaldson Hanna K.L., Bowles N.E. and Russell S.S. (2020)**  
Linking mineralogy and spectroscopy of highly aqueously altered CM and CI carbonaceous chondrites in preparation for primitive asteroid sample return. *Meteoritics and Planetary Science*, **55**, 77–101.
- Browning L., McSween H. and Zolensky M. (1996)**  
Correlated alteration effects in CM carbonaceous chondrites. *Geochimica et Cosmochimica Acta*, **60**, 2621–2633.
- Bunch T.E. and Chang S. (1980)**  
Carbonaceous chondrites – II. Carbonaceous chondrite phyllosilicates and light element geochemistry as indicators of parent body processes and surface conditions. *Geochimica et Cosmochimica Acta*, **44**, 1543–1577.
- Bunch T.E. and Reid A.M. (1975)**  
The nakhlites Part 1: Petrography and mineral chemistry. *Meteoritics*, **10**, 303–315.
- Daly L., Bland P.A., Saxey D.W., Reddy S.M., Fougereuse D., Rickard W.D. and Forman L.V. (2017)**  
Nebula sulfidation and evidence for migration of “free-floating” refractory metal nuggets revealed by atom probe microscopy. *Geology*, **45**, 847–850.



## references

- Daly L., Bland P.A., Tessalina S., Saxey D.W., Reddy S.M., Fougereuse D., Rickard W.D.A., Forman L.V., La Fontaine A., Cairney J.M., Ringer S.P., Schaefer B.F. and Schwander D. (2018) Defining the potential of nanoscale Re-Os isotope systematics using atom probe microscopy. *Geostandards and Geoanalytical Research*, 42, 279–299.
- Daly L., Lee M.R., Bagot P., Halpin J., Smith W., McFadzean S., O'Brien A.C., Griffin S., Hallis L.J. and Cohen B.E. (2020) Exploring Mars at the nanoscale: Applications of transmission electron microscopy and atom probe tomography in planetary exploration. *IOP Conference Series: Materials Science and Engineering*, 891, 012008.
- Dodd R.T. (1981) *Meteorites: A petrologic-chemical synthesis*. CUP Archive. Cambridge University Press (New York, USA).
- Ehlmann B.L., Mustard J.F. and Murchie S.L. (2010) Geologic setting of serpentine deposits on Mars. *Geophysical Research Letters*, 37, L06201.
- Esteban J.J., Cuevas J., Tubia J.M. and Yusta I. (2003) Xonotlite in rodingite assemblages from the Ronda peridotites, Betic Cordilleras, southern Spain. *Canadian Mineralogist*, 41, 161–170.
- Etioppe G., Vadillo I., Whiticar M.J., Marques J.M., Carreira P.M., Tiago I., Benavente J., Jiménez P. and Urresti B. (2016) Abiotic methane seepage in the Ronda peridotite massif, southern Spain. *Applied Geochemistry*, 66, 101–113.
- Fougereuse D., Kirkland C., Saxey D., Seydoux-Guillaume A.-M., Rowles M.R., Rickard W.D. and Reddy S.M. (2020) Nanoscale isotopic dating of monazite. *Geostandards and Geoanalytical Research*, 44, 637–652.
- Fougereuse D., Reddy S.M., Saxey D.W., Rickard W.D., Van Riessen A. and Micklethwaite S. (2016) Nanoscale gold clusters in arsenopyrite controlled by growth rate not concentration: Evidence from atom probe microscopy. *American Mineralogist*, 101, 1916–1919.
- Frost B.R. and Beard J.S. (2007) On silica activity and serpentinisation. *Journal of Petrology*, 48, 1351–1368.
- Fujiya W., Sugiura N., Hotta H., Ichimura K. and Sano Y. (2012) Evidence for the late formation of hydrous asteroids from young meteoritic carbonates. *Nature Communications*, 3, 627.
- Greer J., Rout S.S., Isheim D., Seidman D.N., Wieler R. and Heck P.R. (2020) Atom probe tomography of space-weathered lunar ilmenite grain surfaces. *Meteoritics and Planetary Science*, 55, 426–440.
- Hallis L.J., Taylor G.J., Nagashima K., Huss G.R., Needham A.W., Franchi I.A. and Grady M.M. (2012) Hydrogen isotope analyses of alteration phases in the nakhlite Martian meteorites. *Geochimica et Cosmochimica Acta*, 97, 105–119.
- Hamilton V.E., Simon A.A., Christensen P.R., Reuter D.C., Clark B.E., Barucci M.A., Bowles N.E., Boynton W.V., Brucato J.R., Cloutis E.A., Connolly H.C., Donaldson Hanna K.L., Emery J.P., Enos H.L., Fornasier S., Haberle C.W., Hanna R.D., Howell E.S., Kaplan H.H., Keller L.P., Lantz C., Li J.-Y., Lim L.F., McCoy T.J., Merlin F., Nolan M.C., Praet A., Rozitis B., Sandford S.A., Schrader D.L., Thomas C.A., Zou X.-D., Lauretta D.S. and OSIRIS-REx Team (2019) Evidence for widespread hydrated minerals on asteroid (101955) Bennu. *Nature Astronomy*, 3, 332–340.
- Heck P.R., Stadermann F.J., Isheim D., Auciello O., Daulton T.L., Davis A.M., Elam J.W., Floss C., Hiller J., Larson D.J., Lewis J.B., Mane A., Pellin M.J., Savina M.R., Seidman D.N. and Stephan T. (2014) Atom-probe analyses of nanodiamonds from Allende. *Meteoritics and Planetary Science*, 49, 453–467.
- Hellman O.C., Vandenbroucke J.A., Rüsing J., Isheim D. and Seidman D.N. (2000) Analysis of three-dimensional atom-probe data by the proximity histogram. *Microscopy and Microanalysis*, 6, 437–444.
- Howard K.T., Alexander C., Schrader D.L. and Dyl K.A. (2015) Classification of hydrous meteorites (CR, CM and C2 ungrouped) by phyllosilicate fraction: PSD-XRD modal mineralogy and planetesimal environments. *Geochimica et Cosmochimica Acta*, 149, 206–222.
- Hutchison R. (2006) *Meteorites: A petrologic, chemical and isotopic synthesis (Volume 2)*. Cambridge University Press (New York, USA).
- Hutchison R., Alexander C.M.O. and Barber D.J. (1987) The Semarkona meteorite: First recorded occurrence of smectite in an ordinary chondrite and its implications. *Geochimica et Cosmochimica Acta*, 5, 1875–1882.
- Imae N. and Ikeda Y. (2007) Petrology of the Miller Range 03346 nakhlite in comparison with the Yamato-00593 nakhlite. *Meteoritics and Planetary Science*, 42, 171–184.
- iMOST (2018) The potential science and engineering value of samples delivered to Earth by Mars sample return. (co-chairs Beaty D.W., Grady M.M., McSweeney H.Y., Sefton-Nash E., documentary Carrier B.L., plus 66 co-authors). *White paper, posted August 2018 by MEPAG*, 186pp. <https://mepag.jpl.nasa.gov/reports.cfm>
- Kelly T.F. and Larson D.J. (2012) Atom probe tomography. *Annual Review of Materials Research*, 42, 1–31.
- King A.J., Schofield P.F. and Russell S.S. (2017) Type 1 aqueous alteration in CM carbonaceous chondrites: Implications for the evolution of water-rich asteroids. *Meteoritics and Planetary Science*, 52, 1197–1215.





## references

Kitazato K., Milliken R.E., Iwata T., Abe M., Ohtake M., Matsuura S., Arai T., Nakauchi Y., Nakamura T., Matsuoka M., Senshu H., Hirata N., Hiroi T., Pilorget C., Brunetto R., Poulet F., Riu L., Bibring J.-P., Takir D., Domingue D.L., Vilas F., Barucci M.A., Perna D., Palomba E., Galiano A., Tsumura K., Osawa T., Komatsu M., Nakato A., Arai T., Takato N., Matsunaga T., Takagi Y., Matsumoto K., Kouyama T., Yokota Y., Tatsumi E., Sakatani N., Yamamoto Y., Okada T., Sugita S., Honda R., Morota T., Kameda S., Sawada H., Honda C., Yamada M., Suzuki H., Yoshioka K., Hayakawa M., Ogawa K., Cho Y., Shirai K., Shimaki Y., Hirata N., Yamaguchi A., Ogawa N., Terui F., Yamaguchi T., Takei Y., Saiki T., Nakazawa S., Tanaka S., Yoshikawa M., Watanabe S. and Tsuda Y. (2019)

The surface composition of asteroid 162173 Ryugu from Hayabusa2 near-infrared spectroscopy. *Science*, 364(6437), 272–275.

Lauretta D.S., Balram-Knutson S.S., Beshore E., Boynton W.V., Drouet d'Aubigny C., DellaGiustina D.N., Enos H.L., Golish D.R., Hergenrother C.W., Howell E.S., Bennett C.A., Morton E.T., Nolan M.C., Rizk B., Roper H.L., Bartels A.E., Bos B.J., Dworkin J.P., Highsmith D.E., Lorenz D.A., Lim L.F., Mink R., Moreau M.C., Nuth J.A., Reuter D.C., Simon A.A., Bierhaus E.B., Bryan B.H., Ballouz R., Barnouin O.S., Binzel R.P., Botke W.F., Hamilton V.E., Walsh K.J., Chesley S.R., Christensen P.R., Clark B.E., Connolly H.C., Crombie M.K., Daly M.G., Emery J.P., McCoy T.J., McMahon J.W., Scheeres D.J., Messenger S., Nakamura-Messenger K., Righter K. and Sandford S.A. (2017)

OSIRIS-REx: Sample return from asteroid (101955) Bennu. *Space Science Reviews*, 212, 925–984.

Lauretta D.S., Bartels A.E., Barucci M.A., Bierhaus E.B., Binzel R.P., Botke W.F., Campins H., Chesley S.R., Clark B.C., Clark B.E., Cloutis E.A., Connolly H.C., Crombie M.K., Delbó M., Dworkin J.P., Emery J.P., Glavin D.P., Hamilton V.E., Hergenrother C.W., Johnson C.L., Keller L.P., Michel P., Nolan M.C., Sandford S.A., Scheeres D.J., Simon A.A., Sutter B.M., Vokrouhlický D. and Walsh K.J. (2015)

The OSIRIS-REx target asteroid (101955) Bennu: Constraints on its physical, geological and dynamical nature from astronomical observations. *Meteoritics and Planetary Science*, 50, 834–849.

Lee M.R., Bland P.A. and Graham G. (2003)

Preparation of TEM samples by focused ion beam (FIB) techniques: Applications to the study of clays and phyllosilicates in meteorites. *Mineralogical Magazine*, 67, 581–592.

Lee M.R., Brown D.J., Smith C.L., Hodson M.E., MacKenzie M. and Hellmann R. (2007)

Characterization of mineral surfaces using FIB and TEM: A case study of naturally weathered alkali feldspars. *American Mineralogist*, 92, 1383–1394.

Lee M.R., Cohen B.E. and King A.J. (2019b)

Alkali-halogen metasomatism of the CM carbonaceous chondrites. *Meteoritics and Planetary Science*, 54, 3052–3063.

Lee M.R., Cohen B.E., King A.J. and Greenwood R.C. (2019a)

The diversity of CM carbonaceous chondrite parent bodies explored using Lewis Cliff 85311. *Geochimica et Cosmochimica Acta*, 264, 224–244.

Lee M.R. and Lindgren P. (2016)

Aqueous alteration of chondrules from the Murchison CM carbonaceous chondrite: Replacement, pore filling and the genesis of polyhedral serpentine. *Meteoritics and Planetary Science*, 51, 1003–1021.

Lee M.R., MacLaren I., Andersson S.M.L., Kovács A., Tomkinson T., Mark D.F. and Smith C.L. (2015b)

Opal-A in the Nakhla meteorite: A tracer of ephemeral liquid water in the Amazonian crust of Mars. *Meteoritics and Planetary Science*, 50, 1362–1377.

Lee M.R. and Smith C.L. (2006)

Scanning transmission electron microscopy using a SEM: Applications to mineralogy and petrology. *Mineralogical Magazine*, 70, 579–590.

Lee M.R., Tomkinson T., Hallis L.J. and Mark D.F. (2015a)

Formation of iddingsite veins in the Martian crust by centripetal replacement of olivine: Evidence from the nakhlite meteorite Lafayette. *Geochimica et Cosmochimica Acta*, 154, 49–65.

Lee S., Kim Y.M. and Kim Y.J. (2007)

Formation of crystalline silicon in kaolinite by electron beam irradiation and *in situ* heating in the HVEM. *Journal of Electron Microscopy*, 56, 153–155.

Malpas J. (1992)

Serpentine and the geology of serpentinized rocks. In: Roberts B.A. and Proctor J. (eds), *The ecology of areas with serpentinized rocks: A world view*. Kluwer Academic Publishers (Dordrecht, Netherlands), 7–30.

Miller M.K. and Russell K.F. (1992)

An APFIM investigation of a weathered region of the Santa Catharina meteorite. *Surface Science*, 266, 441–445.

Obata M. (1980)

The Ronda peridotite: Garnet-, spinel-, and plagioclase-herzolite facies and the P-T trajectories of a high-temperature mantle intrusion. *Journal of Petrology*, 21, 533–572.

Pedraza A., Galindo-Zaldívar J., Acosta-Vigil A., Azor A., González-Menéndez L., Rodríguez-Fernández L.R. and Ruiz-Constán A. (2016)

Serpentinization-driven extension in the Ronda mantle slab (Betic Cordillera, S. Spain). *Gondwana Research*, 37, 205–215.

Pérez-Huerta A., Laiginhas F., Reinhard D.A., Prosa T.J. and Martens R.L. (2016)

Atom probe tomography (APT) of carbonate minerals. *Micron*, 80, 83–89.

Perna D., Barucci M.A., Ishiguro M., Alvarez-Candal A., Kuroda D., Yoshikawa M., Kim M.-J., Fomasier S., Hasegawa S., Roh D.-G., Müller T.G. and Kim Y. (2017)

Spectral and rotational properties of near-Earth asteroid (162173) Ryugu, target of the Hayabusa2 sample return mission. *Astronomy and Astrophysics*, 599, L1.



## references

- Poulet F., Bibring J.-P., Mustard J.F., Gendrin A., Mangold N., Langevin Y., Avidson R.E., Gondet B. and Gomez C. (2005)  
Phyllosilicates on Mars and implications for early Martian climate. *Nature*, 438, 623–627.
- Reddy S.M., Saxey D.W., Rickard W.D., Fougereuse D., Montalvo S.D., Verberne R. and van Riessen A. (2020)  
Atom probe tomography: Development and application to the geosciences. *Geostandards and Geoanalytical Research*, 44, 5–50.
- Rivkin A.S., Campins H., Emery J.P., Howell E.S., Licandro J., Takir D. and Vilas F. (2015)  
Astronomical observations of volatiles on asteroids. In: Patrick M., Demeo F.E. and Bottke W.F. (eds), *Asteroids IV*. University of Arizona Press (Tucson, AZ), 65–87.
- Sawada H., Okazaki R., Tachibana S., Sakamoto K., Takano Y., Okamoto C., Yano H., Abe M., Hasegawa S. and Noguchi T. (2017)  
Hayabusa2 Sampler: Collection of asteroidal surface material. *Space Science Reviews*, 208, 81–106.
- Saxey D.W., Moser D.E., Piazzolo S., Reddy S.M. and Valley J.W. (2018)  
Atomic worlds: Current state and future of atom probe tomography in geoscience. *Scripta Materialia*, 148, 115–121.
- Schwartz S., Guillot S., Reynard B., Lafay R., Debret B., Nicolle C., Lanari P. and Auzende A.L. (2013)  
Pressure–temperature estimates of the lizardite/antigorite transition in high pressure serpentinites. *Lithos*, 178, 197–210.
- Shau Y. and Peacor D.R. (1992)  
Phyllosilicates in hydrothermally altered basalts from DSDP Hole 504B, Leg 83 – A TEM and AEM study. *Contributions to Mineralogy and Petrology*, 112, 119–133.
- Thompson K., Lawrence D., Larson D.J., Olson J.D., Kelly T.F. and Gorman B. (2007)  
*In situ* site-specific specimen preparation for atom probe tomography. *Ultramicroscopy*, 107, 131–139.
- Tomeoka K. and Buseck P.R. (1985)  
Indicators of aqueous alteration in CM carbonaceous chondrites: Microtextures of a layered mineral containing Fe, S, O and Ni. *Geochimica et Cosmochimica Acta*, 49, 2149–2163.
- Treiman A.H. and Gooding J.L. (1991)  
Iddingsite in the Nakhla meteorite: TEM study of mineralogy and texture of pre-terrestrial (Martian?) alterations. *Meteoritics*, 26, 402.
- Tsuda Y., Yoshikawa M., Abe M., Minamino H. and Nakazawa S. (2013)  
System design of the Hayabusa 2 Asteroid sample return mission to 1999 JU3. *Acta Astronautica*, 91, 356–362.
- Utsunomiya S., Kersting A.B. and Ewing R.C. (2009)  
Groundwater nanoparticles in the far-field at the Nevada test site: Mechanism for radionuclide transport. *Environmental Science and Technology*, 43, 1293–1298.
- Valley J.W., Cavosie A.J., Ushikubo T., Reinhard D.A., Lawrence D.F., Larson D.J., Clifton P.H., Kelly T.F., Wilde S.A., Moser D.E. and Spicuzza M.J. (2014)  
Hadean age for a post-magma-ocean zircon confirmed by atom-probe tomography. *Nature Geoscience*, 7, 219–223.
- Van der Wal D. and Vissers R.L.M. (1996)  
Structural petrology of the Ronda peridotite, SW Spain: Deformation history. *Journal of Petrology*, 37, 23–43.
- Velbel M.A. (2014)  
Stoichiometric reactions describing serpentinization of anhydrous primary silicates: A critical appraisal, with application to aqueous alteration of chondrule silicates in CM carbonaceous chondrites. *Clays and Clay Minerals*, 62(2), 126–136.
- Velbel M.A., Tonui E.K. and Zolensky M.E. (2012)  
Replacement of olivine by serpentine in the carbonaceous chondrite Nogoya (CM2). *Geochimica et Cosmochimica Acta*, 87, 117–135.
- Vurpillot F., Bostel A. and Blavette D. (2000)  
Trajectory overlaps and local magnification in three-dimensional atom probe. *Applied Physics Letters*, 76, 3127–3129.
- White L.F., Darling J.R., Moser D.E., Reinhard D.A., Prosa T.J., Bullen D., Olson D., Larson D.J., Lawrence D. and Martin I. (2017)  
Atomic-scale age resolution of planetary events. *Nature Communications*, 8, 1–6.
- White L.F., Tait K.T., Langelier B., Lymer E.A., Černok A., Kizovski T.V., Ma C., Tschauner O. and Nicklin R.I. (2020)  
Evidence for sodium-rich alkaline water in the Tagish Lake parent body and implications for amino acid synthesis and racemization. *Proceedings of the National Academy of Sciences*, 117, 11217–11219.
- Wilson M. (1999)  
The origin and formation of clay minerals in soils: Past, present and future perspectives. *Clay Minerals*, 34, 7–25.
- Wilson M.D. and Pittman E.D. (1977)  
Authigenic clays in sandstones: Recognition and influence on reservoir properties and paleoenvironmental analysis. *Journal of Sedimentary Petrology*, 47, 3–31.

## Supporting information

The following supporting information may be found in the online version of this article:

Figure S1. Voltage curve and variation in the laser power of the atom probe during the course of the atom probe tomography analysis of serpentine samples RP1 and RP2.

Figure S2. APT  $u/q$  spectra for RP1 with ranged peaks of each element and molecule labelled.

Table S1. Operating conditions of each successful APT analysis, the run number of each sample and sample label are also given.

Table S2. Operating conditions for each failed Ronda APT sample.

Table S3. EDS data for olivine and serpentine in the Ronda Peridotite. All values in % *m/m*.

Supplementary data file. This section contains the raw RHIT files for APT data for RP1 and RP2, and is available here: [https://glamy.sharepoint.com/:f:/g/personal/luke\\_daly\\_glasgow\\_ac\\_uk/EqyNlfqH0LhEiyaCdQbZtK0BM23\\_hyFWs2AJmACOCz\\_VgQ?e=LepPbh](https://glamy.sharepoint.com/:f:/g/personal/luke_daly_glasgow_ac_uk/EqyNlfqH0LhEiyaCdQbZtK0BM23_hyFWs2AJmACOCz_VgQ?e=LepPbh)

This material is available from: <http://onlinelibrary.wiley.com/doi/10.1111/ggr.12382/abstract> (This link will take you to the article abstract).